



Deconvolution of ^{238,239,240}Pu conversion electron spectra measured with a silicon drift detector

Pommé, S.; Marouli, M.; Paepen, J.; Marković, N.; Pöllänen, R.

Published in:
Applied Radiation and Isotopes

Link to article, DOI:
[10.1016/j.apradiso.2017.08.033](https://doi.org/10.1016/j.apradiso.2017.08.033)

Publication date:
2018

Document Version
Publisher's PDF, also known as Version of record

[Link back to DTU Orbit](#)

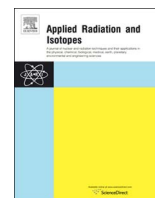
Citation (APA):
Pommé, S., Marouli, M., Paepen, J., Marković, N., & Pöllänen, R. (2018). Deconvolution of ^{238,239,240}Pu conversion electron spectra measured with a silicon drift detector. *Applied Radiation and Isotopes*, 134, 233-239. <https://doi.org/10.1016/j.apradiso.2017.08.033>

General rights

Copyright and moral rights for the publications made accessible in the public portal are retained by the authors and/or other copyright owners and it is a condition of accessing publications that users recognise and abide by the legal requirements associated with these rights.

- Users may download and print one copy of any publication from the public portal for the purpose of private study or research.
- You may not further distribute the material or use it for any profit-making activity or commercial gain
- You may freely distribute the URL identifying the publication in the public portal

If you believe that this document breaches copyright please contact us providing details, and we will remove access to the work immediately and investigate your claim.



Deconvolution of $^{238,239,240}\text{Pu}$ conversion electron spectra measured with a silicon drift detector

S. Pommé^{a,*}, M. Marouli^a, J. Paepen^a, N. Marković^{a,b}, R. Pöllänen^c

^a European Commission, Joint Research Centre, Directorate for Nuclear Safety and Security, Retieseweg 111, B-2440 Geel, Belgium

^b Technical University of Denmark, Center for Nuclear Technologies, Radioecology Department, Roskilde, Denmark

^c Department of Physics, University of Helsinki, P.O. Box 9, FIN-00014, Finland

HIGHLIGHTS

- Performed conversion electron spectrometry with silicon drift detector.
- Deconvoluted conversion electron spectra from $^{238,239,240}\text{Pu}$.
- Alpha deconvolution software applied successfully on ICE spectra.
- ICE emission probabilities in good agreement with BrIcc.

ARTICLE INFO

Keywords:

Plutonium
Isotopic ratio
Nuclear security
Safeguards
Silicon drift detector
Spectrum deconvolution

ABSTRACT

Internal conversion electron (ICE) spectra of thin $^{238,239,240}\text{Pu}$ sources, measured with a windowless Peltier-cooled silicon drift detector (SDD), were deconvoluted and relative ICE intensities were derived from the fitted peak areas. Corrections were made for energy dependence of the full-energy-peak counting efficiency, based on Monte Carlo simulations. A good agreement was found with the theoretically expected internal conversion coefficient (ICC) values calculated from the BrIcc database.

1. Introduction

Plutonium has been investigated from many angles (Clark et al., 2018), among which analytical detection techniques for nuclear security and safeguards is an important one. With the exception of the β^- -emitter ^{241}Pu , the long-lived plutonium isotopes are predominantly alpha emitters. For the determination of plutonium in environmental samples, nuclides of interest are generally ^{238}Pu , ^{239}Pu and ^{240}Pu . Since the intensities of their characteristic gamma-ray emissions are very low, isotopic analysis by gamma spectrometry is a challenge for low activity levels of plutonium. High-resolution alpha-particle spectrometry (Pommé and Sibbens, 2008) is a well-suited alternative technique for measuring isotopic activity ratios in a plutonium mixture, however it suffers from close interferences between the ^{239}Pu and ^{240}Pu peaks and between the ^{238}Pu and ^{241}Am peaks, respectively (see references in Pommé et al., 2016).

A promising alternative technique is spectrometry of the internal conversion electrons (ICE) from the highly converted low-energy gamma transitions following the decay of Pu isotopes. The principle of

the method has been tested with cooled silicon surface barrier detectors (1.8 keV FWHM resolution at 42 keV) (Shiokawa and Suzuki, 1986), windowless Si(Li) detectors (0.48 keV FWHM at 42 keV) (Shiokawa et al., 1990), PIPS detectors cooled (DeVol et al., 2002) or at room temperature (2.2 keV FWHM) (Ahmad et al., 2015), and recently Peltier-cooled silicon drift detectors (SDD, 0.5 keV resolution) (Peräjärvi et al., 2014; Pommé et al., 2016; Dion et al., 2016). It was demonstrated that the ICE peaks from ^{238}Pu , ^{239}Pu , ^{240}Pu and ^{241}Am are well separated in energy. ICE spectrometry is better suited than alpha spectrometry in preserving its capability to determine the $^{240}\text{Pu}/^{239}\text{Pu}$ isotopic ratio as a function of sample thickness (Peräjärvi et al., 2014). However, as a complementary or standalone technique it requires further research on spectrum deconvolution and reference emission data.

In this work, the relative emission probabilities for the L and M+ICE peaks for the 43.469 keV (^{238}Pu), 51.624 keV (^{239}Pu), and 45.244 keV (^{240}Pu) gamma transitions are investigated. To this end, independent deconvolution software tools have been developed at JRC and STUK to fit simultaneously the x-ray and conversion electron peaks obtained with a silicon drift detector. The ICE peak areas are

* Corresponding author.

E-mail address: stefaan.pomme@ec.europa.eu (S. Pommé).

determined and relative intensities are derived. A comparison is made with theoretical calculations and experimental data from literature.

2. Experiment

2.1. ICE spectrometry with an SDD

In previous work, the novel ICE spectrometry set-ups with SDD at STUK and JRC have been described in detail (Peräjärvi et al., 2014; Pommé et al., 2016). They are well suited for measuring low-energy x-rays and electrons. Internal conversion electron (ICE) spectra have been taken of thin plutonium sources, respectively enriched in the isotopes ^{238}Pu , ^{239}Pu , and ^{240}Pu . The spectra show major ICE peaks between 20 and 50 keV, with an energy resolution of 0.5 keV. The shape of the conversion electron energy peaks is comparable to alpha peaks, with typical peak shift and tailing due to energy loss in the absorbing materials. The x-ray energy peaks are comparably sharp and their position is invariable to the thickness of the source and other dead layers. As a result of the difference in peak shift, a separate energy calibration is applied for electron and x-ray peaks.

2.2. Spectral deconvolution

Just as in alpha spectrometry (Pommé, 2015), peak overlap is an issue in ICE spectrometry. It requires the use of spectral deconvolution software which can quantify the full-energy peaks as well as reproduce the continuum underneath the peaks. As suggested in earlier work (Pommé et al., 2016), the analytical functions used in alpha spectrometry are well suited to represent electron peaks with varying degrees of energy straggling. At the JRC, the spreadsheet application 'BEST' (Pommé and Caro Marroyo, 2015) and at STUK, the software 'ADAM' (Pöllänen et al., 2012) were used for spectral analysis. The analytical functions consist of a Gaussian distribution convoluted with exponential tailing functions, the number of which is chosen on the basis of the spectral shape. ADAM allows up to 3 left-handed tailing functions and can fit a continuum underneath the peaks by means of a polynomial function. BEST allows for a higher number of left-handed as well as right-handed exponentials, but fully relies on the peak shapes to cover also the continuum part of the spectrum. The x-ray peaks at 20.2 keV and 20.8 keV were represented by a Gaussian function each (whereas ideally a Voigt function is used and a low-energy continuum added to the peak function). Their intensity ratio was kept fixed at a value of 4.7/1 (Chu et al., 1999).

2.3. Simulation of counting efficiency

The total counting efficiency for the conversion electrons in a silicon detector deviates by about 14–18% (Martin et al., 2013) from the geometrical efficiency due to backscattering against the surface. The backscattering probability depends on the angle of incidence and the energy of the electron. Of the detected particles, a fraction of about 88–91% of the kinetic energy is deposited in the Si crystal and the peak-to-total ratio is about 81–85%. Monte Carlo simulations of particle transport (Salvat and Fernández-Varea, 2009) were performed with Penelope (Salvat et al., 2011) and EGSnrc (Kawrakow and Rogers, 2001) to estimate the energy dependency of the counting efficiency.

2.4. Theoretical calculations with BrIcc

Theoretical values of the ICC, using the frozen-orbital approximation, are available through the database 'BrIcc', which was accessed through a web interface (Kibédi et al., 2008). Input parameters are the daughter nuclides of the Pu isotopes as well as the energy and polarity of their gamma transitions. Some characteristics of the main transitions for $^{238,239,240}\text{Pu}$ are listed in Table 1. The 43.469 keV (^{238}Pu), 51.624 keV (^{239}Pu) and 45.244 keV (^{240}Pu) gamma transitions are

Table 1

ICCs calculated with BrIcc and subsequently derived ICE intensities for 4 gamma transitions in the decay of $^{238,239,240}\text{Pu}$. The gamma transition probabilities are obtained from (DDEP, 2017).

Parent	^{238}Pu	^{239}Pu	^{239}Pu	^{240}Pu
Daughter	^{234}U	^{235}U	^{235}U	^{236}U
Transition (keV)	43.498	51.624	38.661	45.244
$P_{\gamma+ce}$ (%)	28.3 (8)	8.38 (18)	3.56 (21)	27.3 (8)
Polarity	E2	E2	M1 + 22.2% E2	E2
α_T	713 (10)	310 (5)	339 (20)	589 (9)
α_L	520 (8)	226 (4)	249 (14)	429 (6)
α_M	143.5 (20)	62.6 (9)	67 (4)	118.6 (17)
I_{ce} (%)	28.26	8.35	3.55	27.25
$I_{ce,L}$ (%)	20.61	6.09	2.61	19.85
$I_{ce,M}$ (%)	5.69	1.69	0.70	5.49
$I_{ce,N-Q}$ (%)	1.96	0.577	0.24	1.92
$I_{ce,M-Q}$ (%)	7.65	2.26	0.94	7.40

highly converted and have E2 polarity. In the case of ^{239}Pu , a second gamma transition at 38.661 keV with mixed M1 + 22.2% E2 polarity ($\delta = 0.534$ (24)) was taken into account (DDEP, 2017). The ICE intensities were calculated from the ICCs and the gamma transition probability, i.e. $I_{ce,x} = P_{\gamma+ce} \alpha_x / (1 + \alpha_T)$.

3. Results

3.1. Counting efficiency

For the simulation of the full-energy-peak (FEP) detection efficiency, $\varepsilon_p(E)$, the detector was represented as a silicon wafer with 100 mm² area, 500 μm thickness, and 50 nm dead layer. Electrons with energy between 10 and 120 keV were generated from a point or 1-cm-diameter disk source, at 1 cm, 2 cm or 5 cm distance on the symmetry axis, using random angles within the solid angle subtended by the 80 mm² aperture of the circular diaphragm in front of the detector. The simulated detection probabilities for electrons emitted within the aperture are shown in Fig. 1.

Differences in counting efficiency for the different configurations are due to the increasing probability for backscattering with increasing deviation from a perpendicular incidence angle. The angular dependency of the detection efficiency can be approximated by a polynomial function

$$\frac{\varepsilon_p(\theta)}{\varepsilon_p(0)} \approx 1 + a_1\theta + a_2\theta^2 + a_3\theta^3 \quad (1)$$

in which the angle θ (expressed in radian) takes the value 0 for a perpendicular hit. For a silicon disk without dead layer, the angular dependency at $E = 35$ keV simulated with EGSnrc is quasi parabolic between $\theta = 0$ and $\theta = 1$, with $a_1 = 0.0416$ and $a_2 = -0.293$.

The $\varepsilon_p(E)$ values obtained with EGSnrc and Penelope show a similar energy dependency, even though they differ in absolute value by about 1% (see Fig. 1). However, only the detection efficiency ratios among the ICE peaks is of relevance in this work. All data sets, when divided by their reference value at $E = 120$ keV, can be rather well represented by the same polynomial function (see bottom graph of Fig. 1)

$$\frac{\varepsilon_p(E)}{\varepsilon_p(120 \text{ keV})} \approx \exp[a_0 + a_1 \ln(E) + a_2 \ln(E)^2 + a_3 \ln(E)^3] \quad (2)$$

The fit to the EGSnrc $\varepsilon_p(E)/\varepsilon_p(120 \text{ keV})$ data for a point source at 2 cm distance, with $a_0 = -0.594$, $a_1 = 0.39556$, $a_2 = -0.09007$, and $a_3 = 0.006969$, was taken as the reference efficiency curve in this work. The effective thickness of the dead layer is a major source of uncertainty at low energy.

3.2. Spectral deconvolution

The spectra were first subjected to a fit of all ICE peaks in one go,

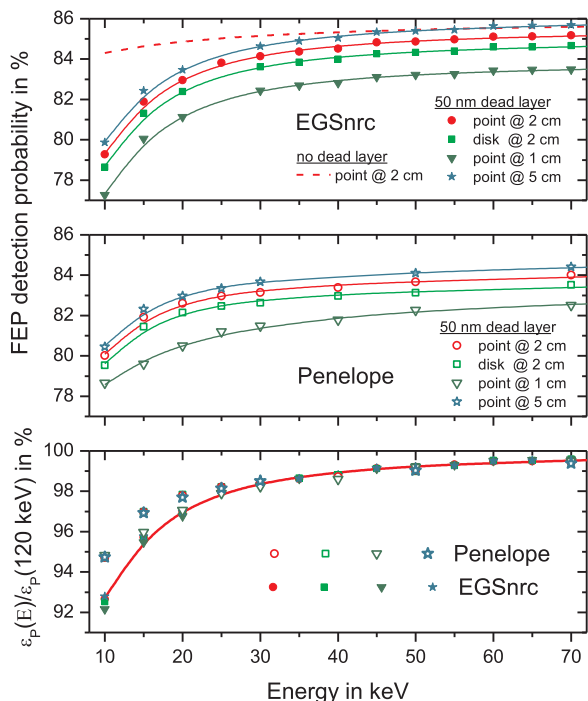


Fig. 1. EGSnrc (top) and Penelope (middle) simulation results for the energy dependence of the FEP detection efficiency for electrons emitted in a cone within the diaphragm aperture of the silicon detector, starting from a point source at 1, 2, 5 cm and a 1-cm-diameter disk source at 2 cm distance, respectively. Differences are due to the angular dependence of the backscattering probability. FEP detection efficiency ratios $\varepsilon_p(E)/\varepsilon_p(120 \text{ keV})$ compared to the reference efficiency curve (bottom).

using the same shaping for all peaks and applying the BrIcc relative intensity values in combination with the fitted energy dependency of the FEP counting efficiency. At first glance, the peak positions and relative areas were rather well reproduced, but for an optimum quality fit the premise of identical shaping parameters for all peaks over the 20–52 keV energy range had to be abandoned. The peaks in the 20–35 keV range showed relatively more tailing than the ones in the higher energy side of the spectrum. Therefore, the L peaks were fitted separately from the M+ peaks with independent shaping parameters.

The good quality of the fits gave a first confirmation that the BrIcc values were compatible with the measurements. In a second iteration, the areas of the major peaks were allowed to fit freely, which improved the quality of the fit slightly. An example is shown in Fig. 2 for ^{239}Pu .

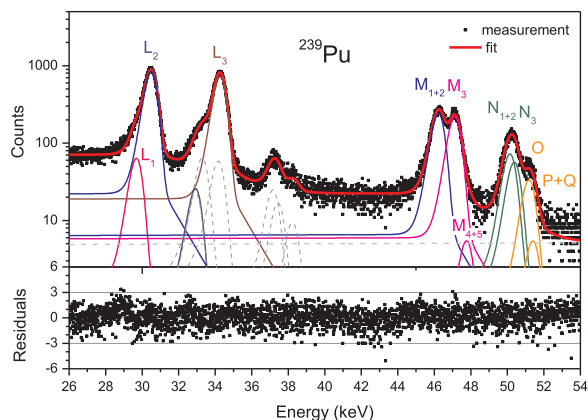


Fig. 2. ICE spectrum of ^{239}Pu measured with a SDD and fitted as a whole with BEST, using fixed shape parameters for all peaks, except for a small linear variation of the peak width σ . The full and dashed lines are fitted ICE peaks of the 51.624 keV and 38.661 keV gamma transitions, respectively. The residuals of the fit are expressed relative to the standard uncertainty of the number of counts in each bin.

The intensity ratio L/M+ was derived from the full spectrum fits, because the fitted amplitudes are proportional to the peak areas only when they correspond to the same shape parameters. Intensity ratios within the L shell (L1/L2/L3) and within the M+ shells was derived from the separate fits over a narrow energy range; Figs. 3–5 show the fit results obtained with BEST for ICE spectra of ^{238}Pu , ^{239}Pu , and ^{240}Pu , respectively. The χ^2 of the L and M+ subshell fits with BEST varied between 1.0 and 1.2. In Fig. 6, the fit result obtained with ADAM is presented in a linear scale for the ^{238}Pu spectrum, showing besides the peaks also the fitted quasi-linear continuum subtracted from the measured areas.

3.3. ICE intensities

In Table 2, an overview is presented of the relative and absolute ICE emission probabilities derived from the spectral deconvolutions, as well as theoretical values from BrIcc and experimental values published by others. The relative ICE intensities were calculated from the ratio of the peak areas (or amplitudes) A , corrected for the energy dependency of the FEP detection efficiency through Eq. (2), e.g. $I_{ce,L2}/I_{ce,L} = (A_{L2}/\varepsilon_{p,L2})/\Sigma(A_{Li}/\varepsilon_{p,Li})$. The absolute intensities were obtained by multiplication with the corresponding subshell intensities $I_{ce,L}$ and $I_{ce,M-Q}$ from Table 1. The results derived from the L spectra, the M+ spectra, and the full spectra are clearly separated in Table 2. Besides individual subshell intensities, also summed intensities of interfering peaks are shown because they could be determined with higher accuracy.

3.4. Uncertainty estimation

The ADAM software performs uncertainty calculation of each peak area through a full covariance calculation (Ihantola et al., 2011). For the results produced by BEST, detailed uncertainty estimation was performed by hand, taking into account three major components:

$$u^2(I_k) = u_{\text{stat}}^2 + u_{\text{intf}}^2 + u_{\text{eff}}^2 \quad (3)$$

in which u_{stat} refers to statistical uncertainties, u_{intf} to correlated uncertainties due to peak and tailing interferences, and u_{eff} to uncertainties due to energy dependency in the FEP detection efficiencies. The corresponding values have been included in Table 2.

The u_{eff} value was estimated roughly as 30% of the difference in FEP efficiency (Eq. (2)) of each peak with the weighted mean of the fitted peaks. Therefore, this uncertainty contribution is relatively smaller for the subshell fits covering a small energy range than for the fits of the complete spectra.

The u_{stat} and u_{intf} standard uncertainty components of ICE spectrometry are similar to those in alpha-particle spectrometry (Pommé, 2015). For the u_{stat} contribution, a pragmatic approach was followed similar to one applied for determinations of alpha-particle emission probabilities (see e.g. Marouli et al., 2014 and Pommé, 2014). The statistical uncertainty for a peak area A_k is approximated through

$$u_{\text{stat}}(A_k) = \sqrt{A_k + 2 \cdot (A_k^t + A_k^f)} \quad (4)$$

in which A_k^t is the (tailing) fraction of the interfering peaks underneath the central part of peak k , and A_k^f represents errors due to imperfections in the peak modelling, taken as the sum of the absolute values of the fit residuals within $\pm 2\text{FWHM}$ of the peak top. The relative intensities I_k within the L and M+ spectra are normalised to 100% and the propagation formula for independent uncertainties is applied for u_{stat} (Pommé, 2015)

$$u^2(I_k) = I_k^2 (1 - I_k)^2 \left(\frac{u^2(A_k)}{A_k^2} + \frac{u^2(\sum_{i \neq k} A_i)}{(\sum_{i \neq k} A_i)^2} \right) \quad (5)$$

Similarly to alpha spectrometry (Pommé, 2015; Marouli et al., 2017), another propagation formula is used to account for anti-

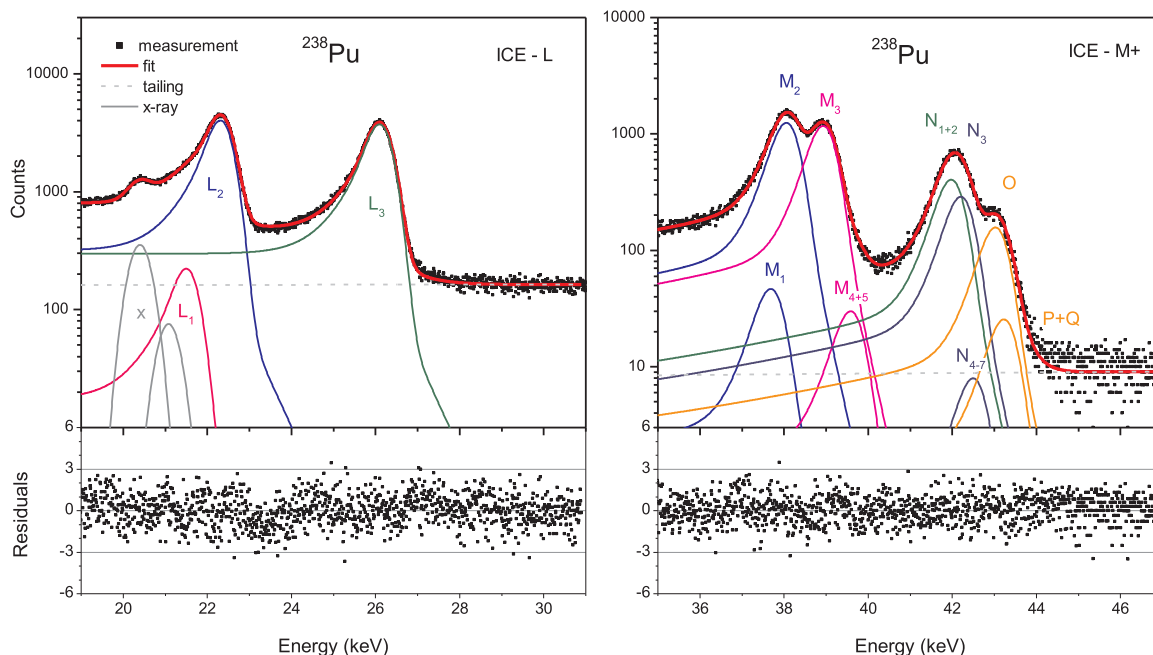


Fig. 3. Independent fits with BEST of the L peaks and the M+ peaks of ²³⁸Pu and residuals of the fits. The residuals of the fit are expressed in standard uncertainty of the number of counts.

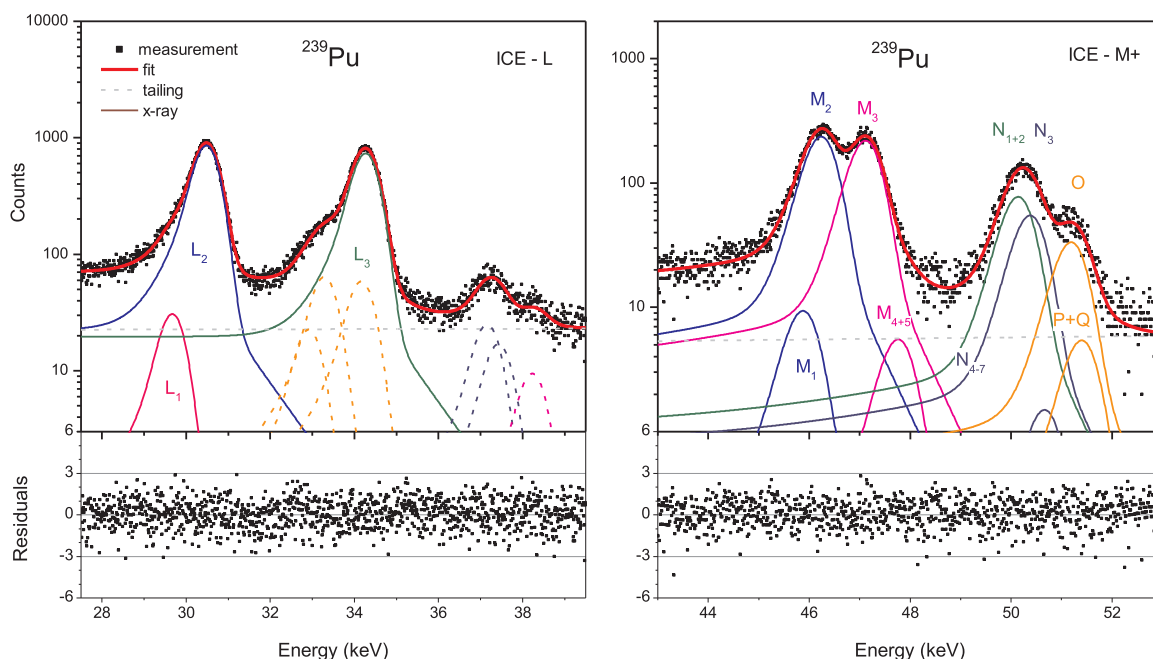


Fig. 4. Independent fits with BEST of the L peaks and the M+ peaks of ²³⁹Pu and residuals of the fits. The residuals of the fit are expressed in standard uncertainty of the number of counts.

correlations between interfering peaks:

$$u^2(I_k) = \left(\frac{u_{\text{inf}}^2(A_k)}{(\sum_i A_i)^2} \right) \quad (6)$$

The interference from peaks *i* underneath the peak *k* was defined as 3% of their area in the region of ± 2FWHM around the top of peak *k*.

4. Discussion

The major relative intensities for L1,2; L3; M1,2; M3,4,5; N, O+ derived from the fit with BEST agree within 0.5–1.5% with the Brlcc data. Even the results of interfered peaks were mostly conforming with Brlcc data within 3

standard uncertainties. The differences between fit results from ADAM and Brlcc were of comparable magnitude, with only a few exceptions amounting up to 2.5%. There is also agreement within 1.3% with the major relative intensities of ²³⁸Pu derived from the measurement results of Amtey et al. (1969). On the other hand, there is poor agreement with the ²³⁸Pu and ²³⁹Pu data produced by Dion et al. (2016); the differences amount up to 5%, even though their measurements were based on the same SDD technique. The L1,2, L3, M, and N+ relative intensities derived from the conversion coefficients of Ahmad et al. (2015) for ²³⁹Pu and ²⁴⁰Pu are consistent with the data in this work, taking into account their uncertainty (typically 2.5%). In the case of ²⁴⁰Pu, the ratio of their published absolute intensities for M and N+ is inconsistent with their ICC values.

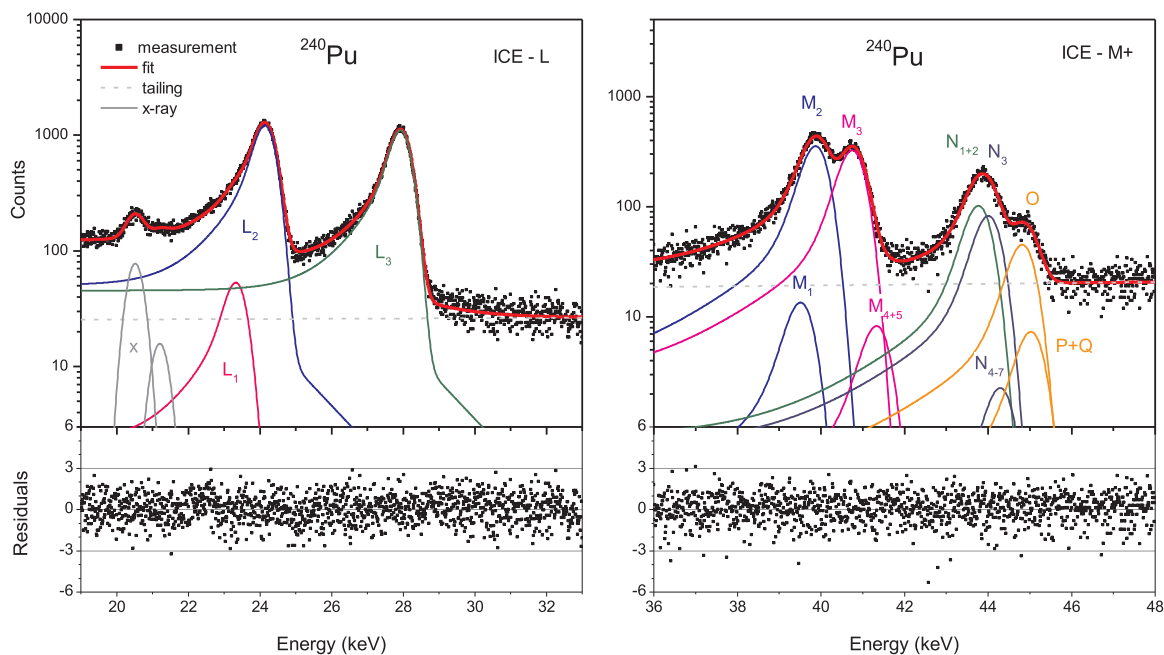


Fig. 5. Independent fits with BEST of the L peaks and the M+ peaks of ^{240}Pu and residuals of the fits. The residuals of the fit are expressed in standard uncertainty of the number of counts.

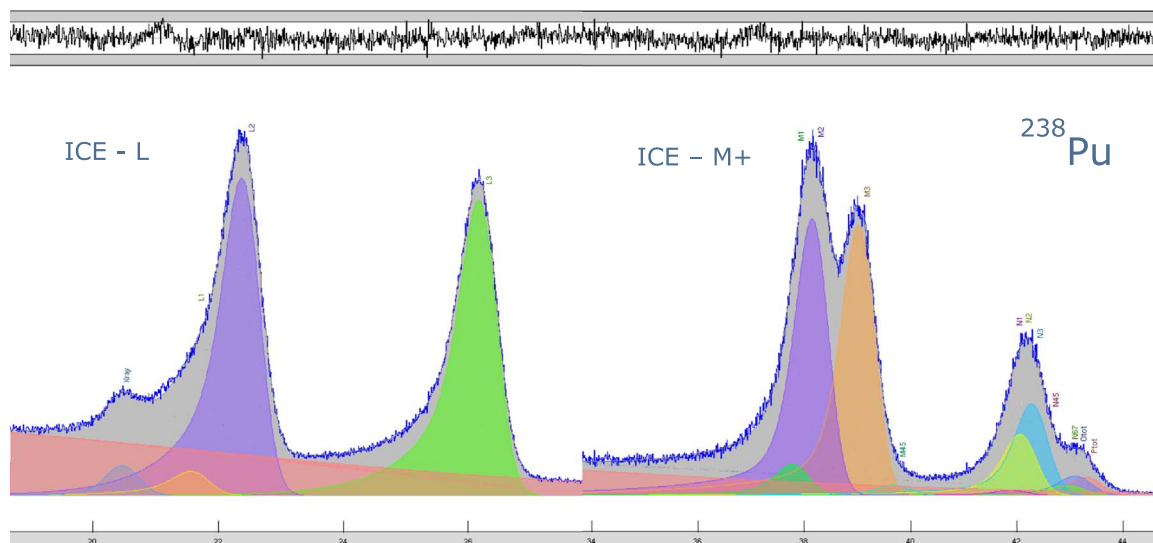


Fig. 6. Independent fits with ADAM of the L peaks and the M+ peaks of ^{238}Pu – including a linear continuum – and residuals of the fits.

Compared to subshell analysis, the deconvolution of a full spectrum is more challenging because of three major issues inherent to covering a wide energy range of about 30 keV: there are significant variations in the FEP detection efficiency, differences in stopping power obstruct the use of fixed peak shape parameters for all ICE peaks, and there is a larger variation in the continuum part underneath the peaks. In this work, two extreme options were applied in which either the major part of the continuum was subtracted through a polynomial function (ADAM) or completely assumed by tailing of the fitted ICE peaks (BEST). The ideal solution may be intermediate between both approaches. As a result of all these difficulties, the intensity ratios between L and M+ shells could not be determined very accurately and the differences with BrIcc data amounted to 0.5–1.5% (BEST). The corresponding ADAM data in Table 2 were deduced from the subshell fits, which is not ideal for direct comparison.

5. Conclusions

The alpha spectrometry software packages ADAM and BEST have been successfully applied for deconvolution of conversion electron spectra from the decay of $^{238,239,240}\text{Pu}$ obtained from thin mononuclidic sources measured with a silicon drift detector. Relative ICE intensities were derived from the spectral fits which agreed within uncertainties with theoretical values from BrIcc and experimental data from Amtey et al. (1969) and Ahmad et al. (2015). They did not agree well with the measurement results by Dion et al. (2016). The major sources of uncertainty are spectral interference, counting statistics, and energy dependence of the detection efficiency, mainly due to backscattering.

For an accurate determination of the emission probabilities, a correction for energy dependence of the detection efficiency should be applied. In this work, Monte Carlo simulations with EGSnrc and Penelope were used to estimate the energy and angular dependence of

Table 2

Relative and absolute emission probabilities of conversion electrons associated with the main gamma transitions following the decay of ^{238,239,240}Pu: (i) subshell, (ii) ICE energy, (iii–v) relative intensity derived from Brlcc and from spectral deconvolution with ADAM and BEST (compensated for FEP detection efficiency ratios), (vi) z-score of BEST result compared to Brlcc ($z = (I_{BEST} - I_{Brlcc})/u(I_{BEST})$), (vii–ix) standard uncertainty components due to counting statistics, peak interferences and differences in FEP efficiency, (x–xii) quantities derived from measurement results published by others, (xiii–xiv) absolute intensities obtained through combination with the probabilities for internal conversion in Table 1. The L', M' and N' intensity values of the 38.66 keV transition (²³⁹Pu) were taken directly from a fit with BEST to the L spectrum of the 51.62 keV transition. BEST results in italic refer to small peaks being fitted at a fixed ratio with an interfering large peak. The χ^2 is an indicator of the goodness of fit in the corresponding energy region.

ICE	Energy keV	I/ΣI			z-score BEST (-)	u (I/ΣI)			I/ΣI			I		
		Brlcc %	Adam %	BEST %		<i>u_{stat}</i> %	<i>u_{intf}</i> %	<i>u_{eff}</i> %	Amtey et al. %	Ahmad et al. %	Dion et al. %	Brlcc %	BEST %	
²³⁸Pu – L spectrum (19–31 keV)													$\chi^2 = 1.23$	
L1	21.74	1.78	3.1	2.8 (21)	0.7	0.14	2.1	0.11	1.82		4.0	0.37	0.6 (5)	
L2	22.55	52.12	50.3	50.3 (25)	- 0.7	0.07	2.5	0.07	52.45		53.7	10.74	10.4 (6)	
L3	26.33	46.15	46.6	47.0 (6)	1.4	0.06	0.6	0.08	45.73		42.3	9.51	9.7 (4)	
ΣL		100										20.6 (6)		
L1,2		53.89	53.5	53.0 (6)	- 1.4	0.07	0.6	0.07	54.27			11.11	10.9 (4)	
L1,2/L3		1.168	1.15	1.13 (3)	- 1.4				1.187 (2)		1.36			
²³⁸Pu – M+ spectrum (35–47 keV)													$\chi^2 = 0.97$	
M1	37.95	1.40	4.0	1.4 (23)		0.22	2.3	0.02	1.5			0.107	<i>0.11 (18)</i>	
M2	38.32	37.40	35.6	37.0 (25)	- 0.2	0.14	2.4	0.02	36.8			2.86	2.82 (21)	
M3	39.19	34.76	34.7	34.7 (23)	0.0	0.13	2.3	0.01	35.4		32.2	2.66	2.65 (20)	
M4,5	39.84	0.89	1.3	0.9 (17)		0.19	1.7	0.00	0.7			0.068	0.07 (13)	
N1,2	42.22	10.46	8.4	11.9 (6)	2.9	0.11	0.6	0.03				0.800	0.91 (5)	
N3	42.45	9.44	11.7	8.5 (9)	- 1.0	0.11	0.9	0.03				0.721	0.65 (7)	
N4	42.74	0.26	1.3	0.2 (8)		0.13	0.8	0.03				0.020	<i>0.02 (6)</i>	
O	43.27	4.62	2.5	4.6 (8)	0.0	0.11	0.7	0.04				0.353	0.35 (6)	
P+	43.47	0.75	0.6	0.8 (7)		0.09	0.6	0.04				0.057	<i>0.06 (5)</i>	
ΣM+		100										7.64 (22)		
M1,2		38.80	39.6	38.3 (6)	- 0.6	0.13	0.5	0.02	38.3			2.96	2.93 (11)	
M3,4,5		35.64	36.0	35.6 (24)	0.0	0.13	2.3	0.01	36.1			2.72	2.72 (20)	
M		74.44	75.5	73.96 (24)	- 1.6	0.08	0.22	0.02				5.69	5.65 (17)	
N		20.18	21.4	20.7 (4)	1.3	0.09	0.4	0.03			16.9	1.54	1.58 (6)	
N+		25.55	24.5	26.04 (24)	1.9	0.08	0.22	0.03				1.95	1.99 (6)	
O+		5.37	3.0	5.4 (8)	0.0	0.11	0.7	0.04				0.410	0.41 (6)	
M2/M3		1.076	1.03	1.06 (14)	- 0.1				1.04 (5)		1.37 (7)			
²³⁸Pu – full spectrum (20–50 keV)													$\chi^2 = 2.32$	
L		72.93	(68.6)	72.46 (43)	- 1.1	0.04	0.39	0.18				20.61	20.5 (6)	
M+		27.07	(31.4)	27.54 (43)	1.1	0.04	0.39	0.18				7.65	7.78 (26)	
L/M		3.624	(2.89)	3.55 (8)	- 1.0				3.61					
L/M+		2.694	(2.18)	2.63 (6)	- 1.1									
²³⁹Pu – L spectrum (25–41 keV)													$\chi^2 = 1.03$	
L1	29.87	1.86	1.6	1.8 (19)	0.0	0.3	1.8	0.05				0.11	0.11 (12)	
L2	30.68	53.27	50.9	51.8 (29)	- 0.5	0.15	2.8	0.03				3.24	3.16 (19)	
L3	34.46	45.04	47.5	46.4 (12)	1.3	0.15	1.1	0.04		48.2 (22)	45.0	2.74	2.83 (10)	
ΣL		100										6.10 (13)		
L1,2		55.13	52.6	53.6 (12)	- 1.2	0.15	1.1	0.03		51.8 (23)	55.0	3.36	3.27 (10)	
L1,2/L3		1.224	1.11	1.16 (5)	- 1.2						1.30 (3)			
L'	17–22											2.604	4.2 (20)	
M'	33–35											0.704	0.60 (15)	
N+'	37–39											0.242	0.21 (5)	
²³⁹Pu – M+ spectrum (42–55 keV)													$\chi^2 = 1.12$	
M1	46.08	1.52	0.0	1.5 (22)		0.51	2.1	0.02				0.034	<i>0.03 (5)</i>	
M2	46.44	38.28	36.2	36.8 (23)	- 0.6	0.33	2.3	0.02				0.862	0.83 (6)	
M3	47.32	34.09	34.6	34.1 (22)	0.0	0.33	2.2	0.01			42.6	0.768	0.77 (6)	
M4,5	47.97	0.86	2.8	0.9 (17)		0.46	1.7	0.00				0.0193	0.019 (40)	
N1,2	50.34	10.76	10.2	12.0 (6)	2.5	0.28	0.5	0.03				0.242	0.271 (15)	
N3	50.58	9.29	9.2	8.5 (9)	- 0.8	0.29	0.9	0.04				0.209	0.192 (21)	
N4	50.86	0.25	0.7	0.2 (9)		0.34	0.8	0.04				0.006	<i>0.005 (20)</i>	
O	51.39	4.65	5.0	5.2 (9)	0.7	0.30	0.8	0.05				0.105	0.117 (19)	
P+	51.60	0.76	1.3	0.8 (8)		0.26	0.7	0.05				0.017	<i>0.019 (17)</i>	
ΣM+		100										2.25 (5)		
M1,2		39.80	36.2	38.2 (6)	- 2.0	0.32	0.46	0.02				0.896	0.861 (26)	
M3,4,5		34.95	37.4	35.0 (23)	0.0	0.33	2.2	0.01				0.787	0.79 (6)	
M		74.88	73.6	73.19 (24)	- 5.6	0.20	0.12	0.02			73.4	1.687	1.65 (4)	
N		20.30	20.1	20.8 (4)	1.2	0.24	0.29	0.04			20.2	0.457	0.468 (14)	
N+		25.71	79.9	26.81 (26)	4.3	0.22	0.12	0.04			26.6	0.579	0.604 (15)	
O+		5.41	6.3	6.0 (9)	0.8	0.29	0.8	0.05				0.122	0.136 (19)	
M2/M3		1.123	1.04	1.08 (14)	- 0.3						1.37 (7)			
²³⁹Pu – full spectrum (25–55 keV)													$\chi^2 = 1.15$	
L		72.90	(72.2)	71.4 (5)	- 3.0	0.11	0.46	0.09				6.09	5.96 (14)	
M+		27.10	(27.8)	28.6 (5)	3.3	0.11	0.46	0.09				2.26	2.39 (7)	
L/M		3.610	(3.53)	3.41 (9)	- 2.3						3.66			
L/M+		2.690	(2.60)	2.49 (6)	- 3.0						2.70			

(continued on next page)

Table 2 (continued)

ICE	Energy keV	I/ΣI			z-score BEST (-)	u (I/ΣI)			I/ΣI			I		
		BrIcc %	Adam %	BEST %		u _{stat} %	u _{intf} %	u _{eff} %	Amtey et al. %	Ahmad et al. %	Dion et al. %	BrIcc %	BEST %	
²⁴⁰Pu – L spectrum (19–35 keV)														
				$\chi^2 = 1.01$										
L1	23.49	1.79	3.1	2.3 (19)	0.4	0.24	1.9	0.09				0.36	0.5 (4)	
L2	24.30	52.45	51.2	51.4 (21)	-0.4	0.12	2.1	0.06				10.41	10.2 (6)	
L3	28.08	45.92	45.7	46.2 (4)	1.2	0.11	0.28	0.07		46.5		9.12	9.2 (3)	
ΣL		100										19.9 (6)		
L1,2		54.24	54.4	53.8 (4)	-1.2	0.12	0.28	0.06		53.5		10.77	10.7 (4)	
L1,2/L3		1.181	1.19	1.16 (2)	-1.2					1.15				
²⁴⁰Pu – M+ spectrum (35–50 keV)														
				$\chi^2 = 1.07$										
M1	39.70	1.42	2.8	1.4 (23)		0.44	2.2	0.02				0.105	0.11 (17)	
M2	40.06	37.54	37.2	37.7 (24)	0.1	0.28	2.4	0.02				2.77	2.78 (20)	
M3	40.94	34.59	34.0	34.5 (23)	0.0	0.28	2.2	0.01				2.55	2.54 (19)	
M4,5	41.59	0.88	0.4	0.9 (17)		0.39	1.6	0.00				0.065	0.06 (13)	
N1,2	43.96	10.51	16.5	10.8 (6)	0.6	0.24	0.5	0.03				0.775	0.80 (5)	
N3	44.20	9.41	4.3	8.8 (9)	-0.7	0.25	0.8	0.03				0.694	0.65 (7)	
N4	44.48	0.26	0.0	0.2 (8)		0.29	0.8	0.03				0.019	0.02 (6)	
O	45.01	4.62	3.4	4.8 (8)	0.3	0.25	0.7	0.04				0.341	0.35 (6)	
P+	45.22	0.75	1.3	0.8 (7)		0.23	0.6	0.04				0.055	0.06 (5)	
ΣM+		100										7.37 (22)		
M1,2		38.96	40.0	39.2 (6)	0.3	0.27	0.44	0.02				2.87	2.89 (11)	
M3,4,5		35.47	34.5	35.4 (23)	0.0	0.28	2.3	0.01				2.61	2.61 (19)	
M		74.43	74.5	74.57 (21)	0.6	0.16	0.13	0.02		77.3		5.49	5.50 (17)	
N		20.15	20.8	19.8 (4)	-0.8	0.21	0.29	0.03				1.49	1.46 (6)	
N+		25.52	25.5	25.43 (24)	-0.4	0.20	0.13	0.03		16.3		1.88	1.87 (6)	
O+		5.37	4.7	5.6 (8)	0.3	0.25	0.7	0.04				0.396	0.41 (6)	
M2/M3		1.085	1.09	1.09 (15)	0.1									
²⁴⁰Pu – full spectrum (22.5–50 keV)														
				$\chi^2 = 1.34$										
L		72.84	(72.3)	73.36 (18)	2.4	0.08	0.04	0.15				19.85	20.0 (6)	
M+		27.16	(27.7)	26.64 (19)	-2.8	0.08	0.04	0.15				7.40	7.26 (22)	
L/M		3.617	(3.51)	3.72 (4)	2.7									
L/M+		2.681	(2.62)	2.75 (3)	2.7									

the detection efficiency in a silicon detector. Polynomial functions were defined to reproduce the simulation results. This correction is of less importance when analysing relative intensities in the L subshell and M+ parts of the spectra separately, and also the quality of the spectral fit is better in a narrow energy region because there is less variation in peak shape.

A good functional representation of the asymmetrical ICE peaks is essential, and is expected to be even more crucial when analysing spectra with less good energy resolution. The continuum fractions of the spectrum can be fitted as the result of tailing of the ICE peaks, which seems to yield good spectral fits and realistic relative peak areas. Alternatively, a polynomial function can be fitted to account fully for the continuum part, with the additional risk of distorting the relative areas of the peaks. Possibly, there is room for improvement through an intermediate approach. In a mixed source with presence of a beta emitter, an algorithm for baseline subtraction is deemed unavoidable.

References

- Ahmad, I., Kondev, F.G., Greene, J.P., Zhu, S., 2015. Room-temperature electron spectroscopy of ²³⁹Pu and ²⁴⁰Pu. *Nucl. Instrum. Methods A* 784, 482–485.
- Amtey, S.R., Hamilton, J.H., Ramayya, A.V., Mladjenovic, M.M., Alton, G., 1969. L and M subshell ratios of the 43.5 keV E2 transition in ²³⁸U. *Nucl. Phys. A* 126, 201–208.
- Chu, S.Y.F., Ekström, L.P., Firestone, R.B., 1999. *The Lund/LBNL Nuclear Data Search, Version 2.0*. website: <<http://nucleardata.nuclear.lu.se>>.
- Clark, D.L., Geeson, D.A., Hanrahan Jr., R.J., 2018. *Plutonium Handbook, 2nd edition*. Vol. I–III American Nuclear Society (in press). <http://www.ans.org/pubs/handbooks/plutonium/>.
- DDEP, 2017. *Table of Radionuclides, vol. 1–7, Monographie BIPM-5 BIPM, Sèvres*, website: <http://www.nucleide.org/DDEP_WG/DDEPdata.htm>.
- DeVol, T.A., Ringberg, A.H., Dewberry, R.A., 2002. Isotopic analysis of plutonium using a combination of alpha and internal conversion electron spectroscopy. *J. Radioanal. Nucl. Chem.* 254, 71–79.
- Dion, M.P., Miller, B.W., Warren, G.A., 2016. Alpha and conversion electron spectroscopy of ^{238,239}Pu and ²⁴¹Am and alpha-conversion electron coincidence measurements. *Nucl. Instrum. Methods A* 830, 6–12.
- Ihantola, S., Pelikan, A., Pöllänen, R., Toivonen, H., 2011. Advanced alpha spectrum analysis based on the fitting and covariance analysis of dependent variables. *Nucl. Instrum. Methods A* 656, 55–60.

- Kawrakow, I., Rogers, D.W.O., 2001. *The EGSnrc Code System: Monte Carlo Simulation of Electron and Photon Transport*, Report PIRS-701. National Research Council of Canada, Ottawa.
- Kibédi, T., Burrows, T.W., Trzhaskovskaya, M.B., Davidson, P.M., Nestor Jr., C.W., 2008. Evaluation of theoretical conversion coefficients using BrIcc. *Nucl. Instrum. Methods A* 589, 202–229. Webinterface. <<http://bricc.anu.edu.au/index.php>>.
- Marouli, M., Pommé, S., Jobbágy, V., Van Ammel, R., Paepen, J., Stroth, H., Benedik, L., 2014. Alpha-particle emission probabilities of ²³⁶U obtained by alpha spectrometry. *Appl. Radiat. Isot.* 87, 292–296.
- Marouli, M., Pommé, S., Van Ammel, R., García-Toraño, E., Crespo, T., Pierre, S., 2017. Direct measurement of alpha emission probabilities in the decay of ²²⁶Ra. *Appl. Radiat. Isot.* 125, 196–202.
- Martin, J.W., et al., 2013. Measurement of electron backscattering in the energy range of neutron β decay. *Phys. Rev. C* 68 (055503), 8.
- Peräjärvi, K., Turunen, J., Ihantola, S., Kämäräinen, V., Pommé, S., Pöllänen, R., Siiskonen, T., Sipilä, H., Toivonen, H., 2014. Feasibility of conversion electron spectrometry using a Peltier-cooled silicon drift detector. *J. Radioanal. Nucl. Chem.* 299, 229–234.
- Pöllänen, R., Siiskonen, T., Ihantola, S., Toivonen, H., Pelikan, A., Inn, K., La Rosa, J., Bene, B.J., 2012. Determination of ²³⁹Pu/²⁴⁰Pu isotopic ratio by high-resolution alpha-particle spectrometry using the ADAM program. *Appl. Radiat. Isot.* 70, 733–739.
- Pommé, S., Sibbens, G., 2008. Alpha-particle counting and spectrometry in a primary standardisation laboratory. *Acta Chim. Slov.* 55, 111–119.
- Pommé, S., 2014. High-resolution alpha-particle spectrometry of ²³⁸U. *Appl. Radiat. Isot.* 87, 315–319.
- Pommé, S., Caro Marroyo, B., 2015. Improved peak shape fitting in alpha spectra. *Appl. Radiat. Isot.* 96, 148–153.
- Pommé, S., 2015. Typical uncertainties in alpha-particle spectrometry. *Metrologia* 52, S146–S155.
- Pommé, S., Paepen, J., Peräjärvi, K., Turunen, J., Pöllänen, R., 2016. Conversion electron spectrometry of Pu isotopes with a silicon drift detector. *Appl. Radiat. Isot.* 109, 183–188.
- Salvat, F., Fernández-Varea, J.M., Sempau, J., 2011. *PENELOPE-2011: A Code System for Monte Carlo Simulation of Electron and Photon Transport*. OECD NEA Data Bank/NSC DOC(2011)/5 (OECD Nuclear Energy Agency, Issy-les-Moulineaux, 2011). <<http://www.oecd-nea.org/dbprog/courses/penelope-2011.pdf>>.
- Salvat, F., Fernández-Varea, J.M., 2009. Overview of physical interaction models for photon and electron transport used in Monte Carlo codes. *Metrologia* 46, S112–S138.
- Shiokawa, Y., Suzuki, S., 1986. Application of internal conversion electron spectrometry to analysis of a ²⁴³Cm/²⁴⁴Cm mixture. *J. Radioanal. Nucl. Chem.* 102 (1), 239–246.
- Shiokawa, Y., Suzuki, K., Suzuki, S., Yagi, M., 1990. Determination of isotopic ratios of plutonium and curium by internal conversion electron spectrometry. *J. Radioanal. Nucl. Chem.* 143 (1), 135–141.